

Multimodal plasmonics in fused colloidal networks

Alexandre Teulle¹, Michel Bosman^{2*}, Christian Girard¹, Kargal L. Gurunatha¹, Mei Li³,
Stephen Mann³, Erik Dujardin^{1*}

¹ CEMES CNRS UPR 8011, 29 rue J. Marvig, 31055 Toulouse Cedex 4, France.

² Institute of Materials Research and Engineering, A*STAR (Agency for Science, Technology and Research), 3 Research Link, 117602 Singapore.

³ Centre for Organized Matter Chemistry, School of Chemistry, University of Bristol, Cantocks Close, Bristol BS81TS, United Kingdom.

Table of Contents

1. **Materials and Methods**
2. **TEM of a typical PNN network.**
3. **Fused plasmonic bead strings by e-beam induced welding of PNN**
4. **Plasmonic transmittance of fused nanoparticle chains**
5. **Theoretical model and numerical simulation of EELS signal**
6. **Compared evolution of peak position with aspect ratio in NP chain, fused bead strings and nanorods**
7. **Statistical correlation between SP modes and topological features**
8. **Principal Component Analysis**
9. **TEM and EELS map of a 0.7 μm long PNN fragment for energy loss between 0.35 and 2.45 eV**

1. Materials and Methods

Nanoparticle chain self-assembly: Plasmonic Nanoparticle Networks (PNN) were synthesized by the method reported in references ^{1,2}. Briefly, Au nanoparticles were freshly prepared by the citrate reduction method at a citrate : [AuCl₄]⁻ molar ratio of 5.2 : 1 and diluted to the required concentration with 18 MΩ.cm deionized water. The average diameter of the Au nanoparticles was 12.0 ± 1.1 nm. The assembly of the PNN was performed at room temperature by adding 2-mercaptoethanol (HS(CH₂)₂OH) to the diluted Au nanoparticle solution at a Au nanoparticles : MEA molar ratio of 1 : 5000. The nanoparticle chain assembly is characterized by a color change from pink to purple as the coupled modes emerge. It was monitored by UV-Visible spectrophotometry until completion within 24 to 48 h after mixing.

TEM sample preparation: A 10 μL droplet of fully formed PNN suspension was drop-casted onto 10-nm thick silicon nitride membranes and left to dry in clean environment. A series of 1-minute O₂ plasma cleaning steps were performed to eliminate the mercaptoethanol and citrate capping moieties. Structural TEM analysis was performed using a Philips CM20FEG microscope operated at 100 kV. Particular care was taken to adjust the plasma cleaning step to avoid any damage or modification of the chain morphology compared to unprocessed PNN. Complementary SEM observations were performed on a Zeiss 1540XB Gemini microscope.

Electron energy-loss spectroscopy (EELS): EELS was performed in scanning TEM (STEM) mode using an FEI Titan TEM with Schottky electron source. The microscope was operated at 80 kV, and a STEM convergence semi-angle of 13 mrad was used to form a probe with a diameter of approximately 1 nm. A Wien-type monochromator dispersed the electron beam in energy, and an energy-selecting slit formed a monochrome electron beam with typical full-width at half-maximum values of 70 meV. A Gatan Tridiem ER EELS detector was used for EELS mapping and spectroscopy, applying a 12 mrad collection semi-angle. EELS data was acquired with a modified binned gain averaging routine:³ individual spectra were acquired in 40 ms, using 8 or 16 times on-chip binning. The detector channel-to-channel gain variation was averaged out by constantly changing the readout location and correcting for these shifts after the EELS acquisition was finished. A high-quality dark reference was acquired separately, and used for post-acquisition dark signal correction. Spectra were normalized by giving the maximum of the zero-loss peak (ZLP) unit value, and the ZLP background signal was removed by fitting and subtracting a high-quality background spectrum.

EELS mapping: EELS maps were obtained with the Spectrum Imaging technique: scanning a small electron probe with an approximate diameter of 1 nm in a rectangular raster of pixels, while at each pixel an EELS spectrum is collected and stored. After data processing as described above, 0.1 eV energy

windows around the plasmon peaks of interest were used to image the EELS intensity in each pixel in linear scale. The EELS intensity maps were colour-coded to a temperature scale.

Simulations: Our model formulates the energy yielded by a swift electron passing in the vicinity of a metallic object in terms of an effective dipole oscillating at the loss frequency. The average power transferred to the plasmonic system is computed by the Green Dyadic Method in which the whole dyad $S(\mathbf{r}, \mathbf{r}', \omega_0)$ of the considered system is calculated by solving a Dyson's equation sequence.⁴ In order to optimize the representation of the complex curved surfaces of the fused bead chains, the volume of the system is discretized in a face centered cubic lattice. This method allows the numerical computation of EELS maps in planes located 10 nm above the top of the nanoparticles for a given energy, $\hbar\omega_0$, and spectra for a fixed position, $\mathbf{R}_0 = (X_0, Y_0, Z_0)$.

NOTE: This method is closely related to the one used to describe an optical excitation of plasmonic nanostructures such as PNN which we described in an earlier work.⁵ In this case other parameter can be explored such as the polarization of the exciting field

2. TEM image of a typical self-assembled PNN network.

The self-assembly driven by the addition of mercaptoethanol (MEA) to citrate-stabilized Au nanoparticles leads to large (2-3 micrometer diameter) globular networks of single particle chains (PNN, Plasmonic Nanoparticle Networks) that can be deposited onto various substrates including TEM grids. The combined collapse and fragmentation of the PNN can be controlled by substrate treatments⁶ and can lead to flat spread chain networks of varying particle density as can be seen in Figure S1. In this work, specific attention was paid to rather small PNN fragments for EELS spectroscopy and mapping. Example of such small broken-off fragments can be seen on the periphery of Fig. S1A.

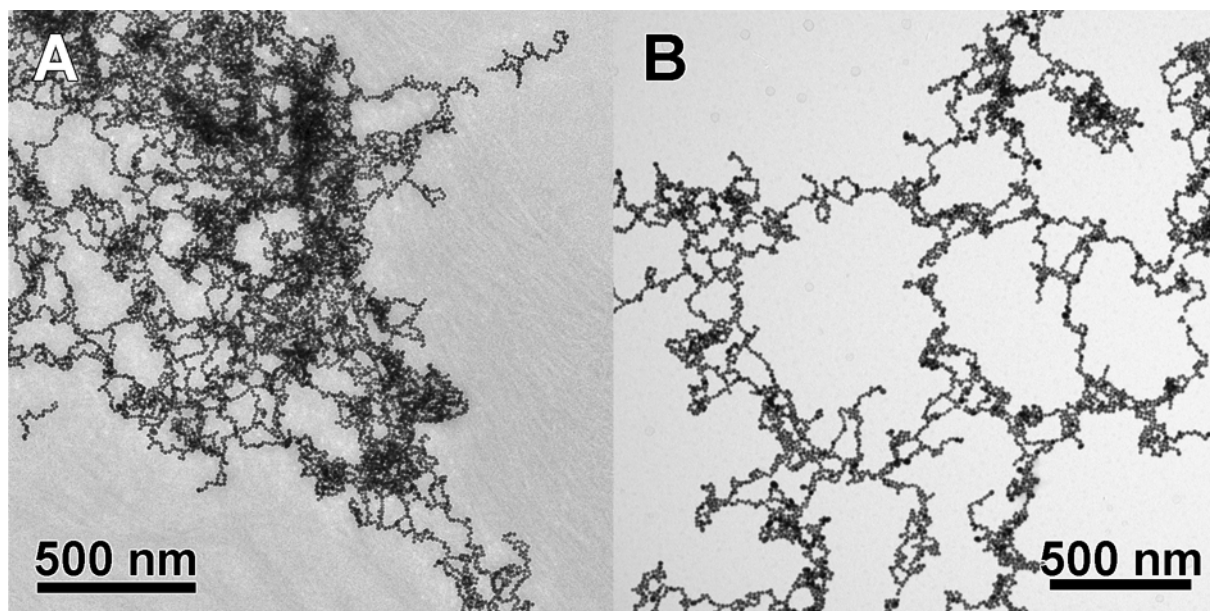


Figure S1: (A, B) Low magnification TEM images of portions of full PNN deposited on carbon film.

3. Fused plasmonic bead strings by e-beam induced welding of PNN

When PNN are deposited on TEM grids with a formvar / carbon film or on SiN or SiO₂ membranes and imaged at 80-120 kV, no significant alteration of the nanoparticles is observed and ample time is allowed to perform structural analysis of the networks as illustrated in Fig. S2A. The self-assembled nanoparticles are initially separated by a 1 nm gap filled with organic molecules (MEA and citrate) that hinder the electron-beam-induced intergrowth.

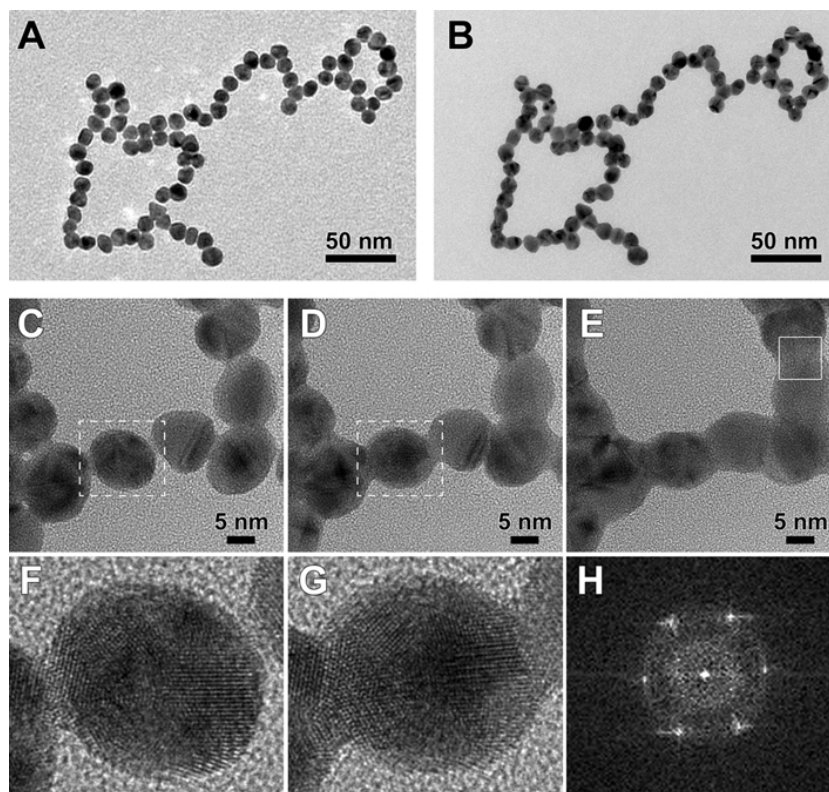


Figure S2. Electron beam induced fusion of PNN. (A, B) TEM images of a PNN fragment (A) before O₂ plasma cleaning at 80 kV and (B) after O₂ plasma cleaning and a few seconds imaging at 200 kV. (C-E) Time-lapsed TEM imaging showing the beam induced fusion of the interfacial areas but preserving the nanoparticle crystallinity. The time intervals are (C-D) 1.3 minutes and (D-E) 4.0 minutes. (F, G) Detail from areas framed in (C, D) showing the crystallinity of the metal bridges formed between neighboring particles during the fusion. (H) Digital Fourier filtering of the interparticle area boxed in (E) after extensive exposure to the electron beam. It shows the six spot of the first Brillouin zone of crystalline gold.

However, when an O₂ plasma is performed in order to remove the capping citrate and MEA molecules prior to TEM imaging at 80 or 200 kV, immediate melting of the interparticle spaces can be observed as in Fig. S2B. After the O₂ plasma and with the possible influence of the underlying SiN_x substrates, the bare and crystalline metal surfaces in close contact are more easily prone to fusion.

This electron-beam induced fusion was exploited in this work to convert self-assembled PNN into fused particle strings where most particles are linked to their nearest neighbors by crystalline Au bridges resulting from the interfacial welding. The sequence of TEM images in Figs. S2C-E illustrates how PNN are transformed into continuous metallic bead strings and shows that the extent of fusion can be controlled by the electron dose. Close-ups of the gap regions of Figs. S2C and S2D are shown in Figures S2F and S2G. Clearly, the gaps on either side of the particle are rapidly filled with crystalline gold as further underlined by the hexagonal patterned shown in Fig. S2H obtained by Fast Fourier filtering of the boxed gap region in Fig. S2E.

The series of images D-E-F illustrates how the adjustment of the time exposure to the electron beam enables to tune the extent of the welding and the final morphology of the fused bead strings.

4. Plasmonic transmittance of fused nanoparticle chains

In this work, fused PNN are conceived as possible plasmonic waveguides with extremely narrow width (e.g. 10 nm) and propagation length in the multi-micrometer length scale when exploiting the lower energy SP modes identified by EELS. While the experimental testing of this proposal is still beyond the capabilities of any available techniques, we have applied our GDM numerical tools that faithfully account for the EELS spatial and spectral data to the calculation of the plasmonic transmittance through a fused nanoparticle chain.

The model systems consists of a linear chain of 5 or 6 Au nanoparticles (diameter 12 nm) similar to those observed in fused PNN. Fig S3A depicts the input-chain-output system. The chain is excited by an optical dipolar source aligned with the chain and placed 12 nm away from the first particle surface. The spectral distribution of the transmitted near-field intensity is calculated at a distal point aligned with the chain located 12 nm away from the last nanoparticle. Figure S3B shows such spectra for two chains lengths of five (blue) and six (green) fused nanoparticles.

The first striking result is that the transmitted intensity is non-zero, suggesting that fused nanoparticle chains do indeed propagate light in a deep sub-wavelength regime. Moreover, the spectral features of the transmitted light present a modal structure that is influenced by the chain length. The relative weight of these modes tends to favor lower energy modes and the resonances are red shifted as the length increases. For example, see the reduced intensity of the 780, 850 nm peaks and increasing intensities of the 920 and 1050 nm peaks plus the emergence of the 1300 nm peak when increasing from five to six particles.

Near field images can be computed just above the chain surface as shown in the inset of Fig. S3B. When the structure is excited off resonance (ex.: 600 nm), the intensity remains located within the first few nanoparticles. However, when a low energy resonance is excited (ex.: 914 nm), a strong intensity is measured at the distal particle illustrating the delocalization of the modal energy. Interestingly, the transmittance does not require that the energy is continuously distributed along the chain but rather that the modal feature excited at that energy presents some finite presence probability at the chain extremity.

This numerical work further confirms that fused PNN do have the potential of efficiently propagating light energy in a deep sub-wavelength regime.

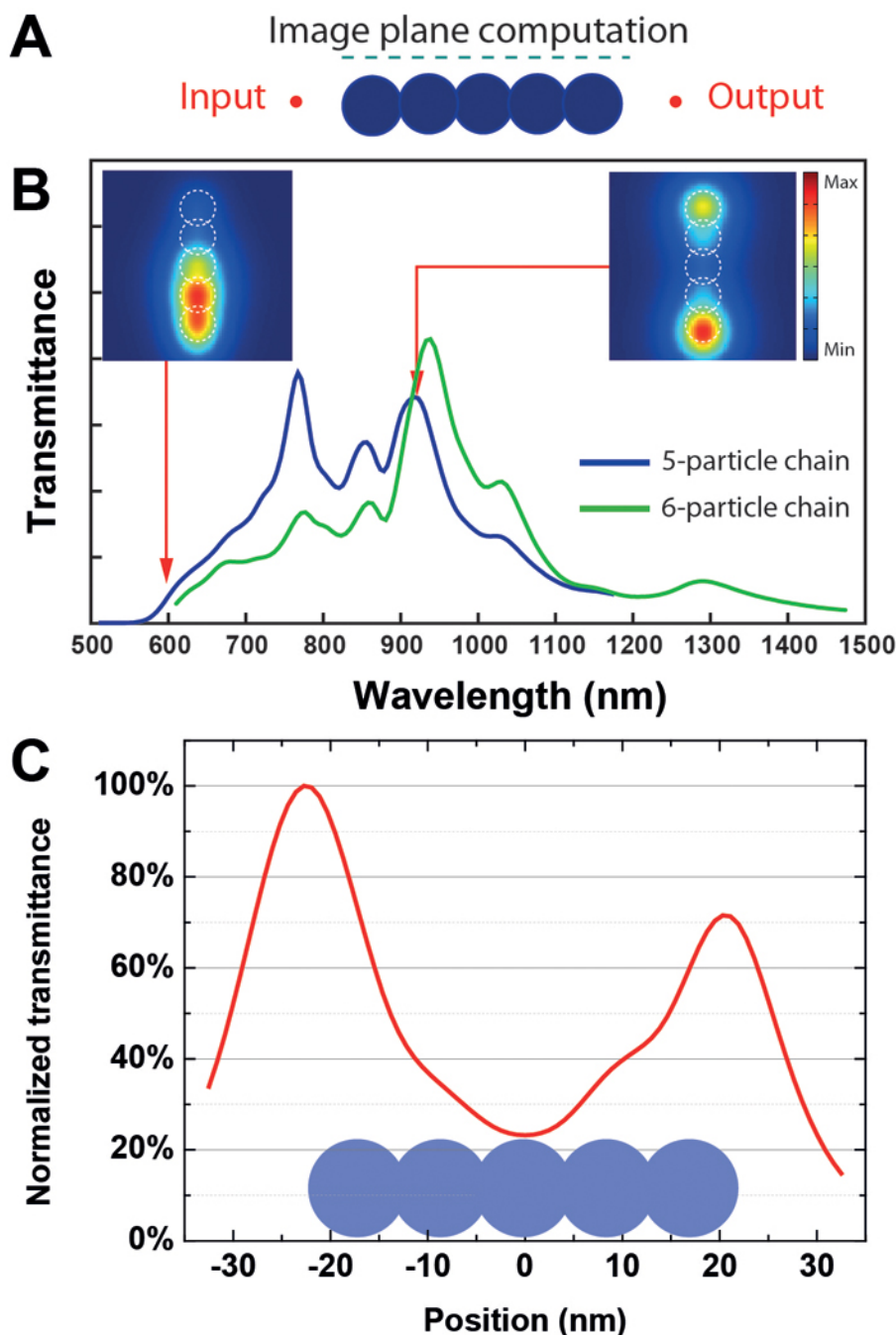


Figure S3. Plasmonic transmittance of fused gold particle chains computed from the Green Dyadic Method (GDM). **(A)** Schematics of the input-chain-output system in which the input is excited by an optical dipolar source aligned along the chain axis and the output signal is the near-field intensity generated by the excited plasmonic field. The nanoparticle diameter is 12 nm and the interparticle pitch is 10 nm. **(B)** Transmittance spectra of five- (blue) and six- (green) particle chains. Two near-field optical images have been computed above the 5-particle structure (see the image computation plane depicted in **(A)**) for two selected excitation wavelengths (off-resonant: 600 nm and resonant: 914 nm). The image size is 65×65 nm. **(C)** Transmission profile along the chain axis of the resonant image (right inset in **(B)**) that shows a transmitted near-field intensity that exceed 70% of the near-field intensity at the input.⁷

5. Theoretical model and numerical simulation of EELS signals

The theoretical description of EELS phenomena recorded in the vicinity of plasmonic particles can be obtained from the photonic LDOS projected onto the electron trajectory. This statement, demonstrated in reference ⁸, proceeds from the computation of the total Coulomb force work accumulated during the electron motion.

In this report, we apply an alternative procedure based on a pure Fermi golden rule approach.

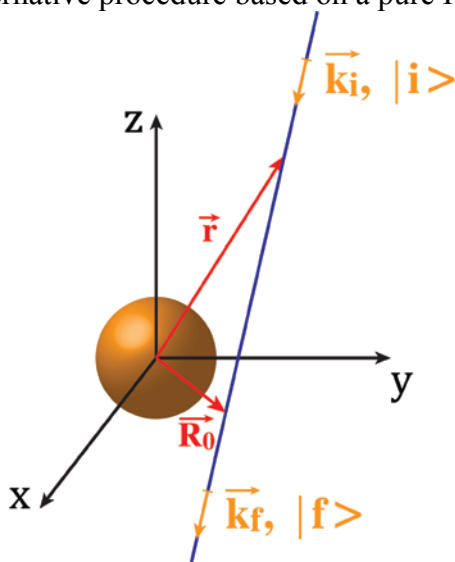


Figure S4. Schematic view of a straight electron trajectory passing near a spherical metal particle.

To illustrate how a fast electron can convert a portion ΔE_0 of its kinetic energy into plasmon oscillations, let us consider the schematic drawing depicted in Figure S4. An inelastic event between electron and particle is equivalent to a transition between a first occupied electronic state $|i\rangle$ and a final unoccupied state $|f\rangle$ of the moving electron. The two Bohr frequencies, ω_i and ω_f , associated with $|i\rangle$ and $|f\rangle$ must verify $\omega_i \geq \omega_f$. The matrix element of the current density associated with this electronic transition is given by the usual relation: ⁹

$$\mathbf{J}_{i,f}(\mathbf{r}, t) = -\frac{ie\hbar}{2m} \{ \nabla_r \psi_f^*(\mathbf{r}, t) \psi_i(\mathbf{r}, t) - \psi_f^*(\mathbf{r}, t) \nabla_r \psi_i(\mathbf{r}, t) \} \quad (1)$$

where m and e are the electron mass and charge, and $\psi_{i/f}$ defines both electronic wavefunctions corresponding to initial and final states $|i\rangle$ and $|f\rangle$, respectively. In the stationary regime corresponding to a constant velocity of the probing electron, before and after the energy transfer event, the electronic wavefunctions display monochromatic oscillation terms:

$$\psi_f(\mathbf{r}, t) = e^{i\omega_f t} \Phi_f(\mathbf{r}) = e^{i(\omega_i - \omega_0)t} \Phi_f(\mathbf{r}) \quad (2)$$

and

$$\psi_i(\mathbf{r}, t) = e^{i\omega_i t} \Phi_i(\mathbf{r}) \quad (3)$$

in which, $\omega_0 = \Delta E_0 / \hbar$ is the angular frequency that corresponds to the energy transferred by the swift electron to the plasmonic system and $\Phi_i(\mathbf{r})$ and $\Phi_f(\mathbf{r})$ define the spatial parts of the electronic wavefunctions, before and after the interaction. After replacing equations (2) and (3) into (1), we can express the real part of the inelastic current as follows:

$$\mathbf{J}_{i,f}(\mathbf{r}, t) = \frac{e\hbar}{2m} A(\mathbf{r}) \cos(\omega_0 t + \Theta(\mathbf{r})), \quad (4)$$

in which, $A(\mathbf{r})$ and $\Theta(\mathbf{r})$ are the modulus and the argument of the complex vector defined by:

$$i\{(\nabla_r)\Phi_f^*(\mathbf{r})\Phi_i(\mathbf{r}) - \Phi_f^*(\mathbf{r})(\nabla_r\Phi_i(\mathbf{r}))\}. \quad (5)$$

From equation (4), the inelastic current can be expanded in Fourier integral:

$$\mathbf{J}_{i,f}(\mathbf{r}, t) = \int \mathbf{J}_{i,f}(\mathbf{r}, \omega) e^{i\omega t} d\omega, \quad (6)$$

with

$$\mathbf{J}_{i,f}(\mathbf{r}, \omega) = \frac{e\hbar}{2m} A(\mathbf{r}) \{\delta(\omega_0 + \omega) e^{i\Theta(\mathbf{r})} + \delta(\omega - \omega_0) e^{-i\Theta(\mathbf{r})}\}, \quad (7)$$

which is associated with the following polarization vector:¹⁰

$$\mathbf{P}_{i,f}(\mathbf{r}, \omega) = \frac{ie\hbar}{2m\omega} A(\mathbf{r}) \{\delta(\omega_0 + \omega) e^{i\Theta(\mathbf{r})} + \delta(\omega - \omega_0) e^{-i\Theta(\mathbf{r})}\}. \quad (8)$$

According to equation (5), the $A(\mathbf{r})$ vectorial function is built from the product of both electron wavepackets expected before (i) and after (f) the elementary inelastic process occurs. Consequently, it can be schematized by a delta Dirac distribution centered around a location $\mathbf{R}_0 = (X_0, Y_0, Z_0)$ defining the position where the electron released an energy quantum $\hbar\omega_0$:

$$A(\mathbf{r}) = A\delta(\mathbf{r} - \mathbf{R}_0); \quad (9)$$

in which the modulus A of the vector $A(\mathbf{r})$ has the dimension of an inverse length. This last relation indicates that each inelastic elementary event occurring at the location \mathbf{R}_0 of the electron trajectory can be represented by an effective dipole fluctuating at the loss-frequency ω_0 :

$$p_{if}(\omega) = \frac{ie\hbar A}{2m\omega} \{\delta(\omega_0 + \omega) + \delta(\omega - \omega_0)\}, \quad (10)$$

in which the phase origin $\Theta(\mathbf{R}_0) = 0$ has been chosen equal to zero for $\mathbf{r} = \mathbf{R}_0$. Now to derive the portion of energy $\Delta E_{EELS}(\omega_0)$, per unit time, transferred by the electron to the metal particle, we just have to apply the laws of electrodynamics of an effective pointlike dipolar light source $p_{if}(t)$, located at \mathbf{R}_0 . Thus, by applying dynamical Gauss' theorem to $p_{if}(t)$ (cf. reference¹⁰), we can write:

$$\Delta E_{EELS}(\omega_0) = \frac{\omega_0 p^2}{2} \mathbf{U} \mathbf{U} : \Im \mathbf{S}(\mathbf{R}_0, \mathbf{R}_0, \omega_0), \quad (11)$$

where p is the dipole amplitude defined by:

$$p = \frac{e\hbar A}{2m\omega_0}, \quad (12)$$

\mathbf{U} defines its orientation, and $\mathbf{S}(\mathbf{R}_0, \mathbf{R}_0, \omega_0)$ labels the field-susceptibility of the metal particle.

Let us note, that in the particular case where the electron travels on a trajectory parallel to the OZ axis, equation (11) reads:

$$\Delta E_{EELS}^z(\omega_0) = \frac{e^2 \hbar^2 A^2}{8m^2 \omega_0} \Im \{ \mathbf{S}_{zz}(\mathbf{R}_0, \mathbf{R}_0, \omega_0) \}, \quad (13)$$

where $S_{zz}(\mathbf{R}_0, \mathbf{R}_0, \omega_0)$ represents the (zz) component of the dyadic tensor \mathbf{S} . The field-propagator $\mathbf{S}(\mathbf{r}, \mathbf{r}', \omega)$ between two arbitrary points \mathbf{r} and \mathbf{r}' enables to know how the electric field, at location \mathbf{r} , is modified near a solid body when a punctual dipolar source is placed in \mathbf{r}' .

Two cases can be considered.

- (i) In the case of a single small metallic particle located at the origin of the framework as depicted in Figure S3, the field propagator $\mathbf{S}(\mathbf{r}, \mathbf{r}', \omega_0)$ can be composed from the field propagator in vacuum $\mathbf{S}_0(\mathbf{r}, \mathbf{r}', \omega_0)$ and the dipolar polarizability:¹¹

$$\mathbf{S}(\mathbf{r}, \mathbf{r}', \omega_0) = \mathbf{S}_0(\mathbf{r}, \mathbf{0}, \omega_0) \cdot \alpha(\omega_0) \cdot \mathbf{S}_0(\mathbf{0}, \mathbf{r}', \omega_0), \quad (14)$$

where $\mathbf{r} = (x, y, z)$ and $\mathbf{r}' = (x', y', z')$. In this latter expression, the vacuum field-susceptibility has been neglected since it does not contribute to the loss of energy.

In a cartesian frame, the (β, γ) components of \mathbf{S}_0 are given by the analytical relation:¹⁰

$$S_{0\beta,\gamma}(\mathbf{r}, \mathbf{0}, \omega_0) = S_{0\beta,\gamma}(\mathbf{0}, \mathbf{r}, \omega_0) = \exp(ik_0 r) \times \frac{3r_\beta r_\gamma - r^2 \delta_{\beta,\gamma}}{r^5}, \quad (15)$$

with $k_0 = \omega_0 / c$, $(r_1 = x, r_2 = y, r_3 = z)$, and $r = \sqrt{x^2 + y^2 + z^2}$.

In the absence of dispersion spatial effects, the dipolar polarizability of a single metallic sphere of radius $a \ll \lambda_0 = 2\pi c / \omega_0$ placed in vacuum, reads:

$$\alpha(\omega_0) = a^3 \left(\frac{\varepsilon_m(\omega_0) - 1}{\varepsilon_m(\omega_0) + 2} \right), \quad (16)$$

where $\varepsilon_m(\omega_0)$ is the permittivity of the metal.

Expression (13) can be easily applied to an assembly of dipoles using the self consistent scheme based on the discrete dipole approximation (DDA) approach described in ref¹¹.

- (ii) For arbitrary shaped metallic particles, the computation of the field-susceptibility $\mathbf{S}(\mathbf{r}, \mathbf{r}', \omega_0)$ requires a volume discretization of the active region (metal). Thus, the plasmonic system is generally sampled into n identical elementary regions of respective centers \mathbf{r}_j and equal volume v , that leads to the following Dyson equation fulfilled by the field-susceptibility $\mathbf{S}(\mathbf{r}, \mathbf{r}', \omega_0)$:¹²

$$\mathbf{S}(\mathbf{r}, \mathbf{r}', \omega_0) = \mathbf{S}_0(\mathbf{r}, \mathbf{r}', \omega_0) + \eta(\omega_0) \sum_{j=1}^n \mathbf{S}_0(\mathbf{r}, \mathbf{r}_j, \omega_0) \cdot \mathbf{S}(\mathbf{r}_j, \mathbf{r}', \omega_0), \quad (17)$$

in which $\eta(\omega_0) = \frac{\varepsilon_m(\omega_0) - 1}{4\pi} v$ is homogeneous to a dipolar polarisability and is directly related to the discretization volume v , that itself depends on the discretization grid used to mesh the particles. For a face-centered cubic lattice, this factor reads $v = b^3 / \sqrt{(2)}$, where b represents the distance between two consecutive discretization cells. The self-consistent equation (17) is solved using the numerical Dyson's equation sequence procedure detailed in reference⁴. This allows the computation of the field-susceptibility $S_{zz}(\mathbf{R}_0, \mathbf{R}_0, \omega_0)$ anywhere outside the source region, and the calculation of the EELS signal according to eq (13).

6. Compared evolution of peak position with aspect ratio in NP chain, fused bead strings and nanorods

Figure S5 compiles experimental data of the position of (i) the longitudinal SP mode in Au nanorods stabilized by CTAB/DDAB (diameter 10 nm, refractive index ca. 2) in aqueous solution, (ii) the longitudinally coupled SP mode in short linear chains of nanoparticles (diameter 64 nm) coated with CTAB/DNA (estimated refractive index ca. 1.3) and separated by 1 nm gaps and (iii) calculated longitudinal SP mode in linear fused bead strings (diameter 12 nm, no molecular coating, medium is air) as depicted in Fig. 3. The experimental and calculated longitudinal SP modes in Au nanorods red-shift linearly with the increasing aspect ratio. On the contrary, the longitudinally coupled SP mode in assembled nanoparticle chains is sub-linear for aspect ratio exceeding 3 and rapidly saturates as reported also in references ^{1,2}. The observation of this mode is made possible by the large local optical index of the organic capping layer that shifts the resonance in the range where the dissipative part of the gold dielectric response is minimal (700-800 nm).¹³ The calculated red-shifting upon increasing the aspect ratio of the fused bead strings between 1 and 4 is linear but the rate is intermediate between those observed from nanorods and assembled nanoparticle chains.

This observation suggests that longitudinal SP modes in fused bead strings are delocalized but sensitive to the surface corrugation inherited from the native PNN, and still present after fusion, which is rougher than the surface of Au nanorods.

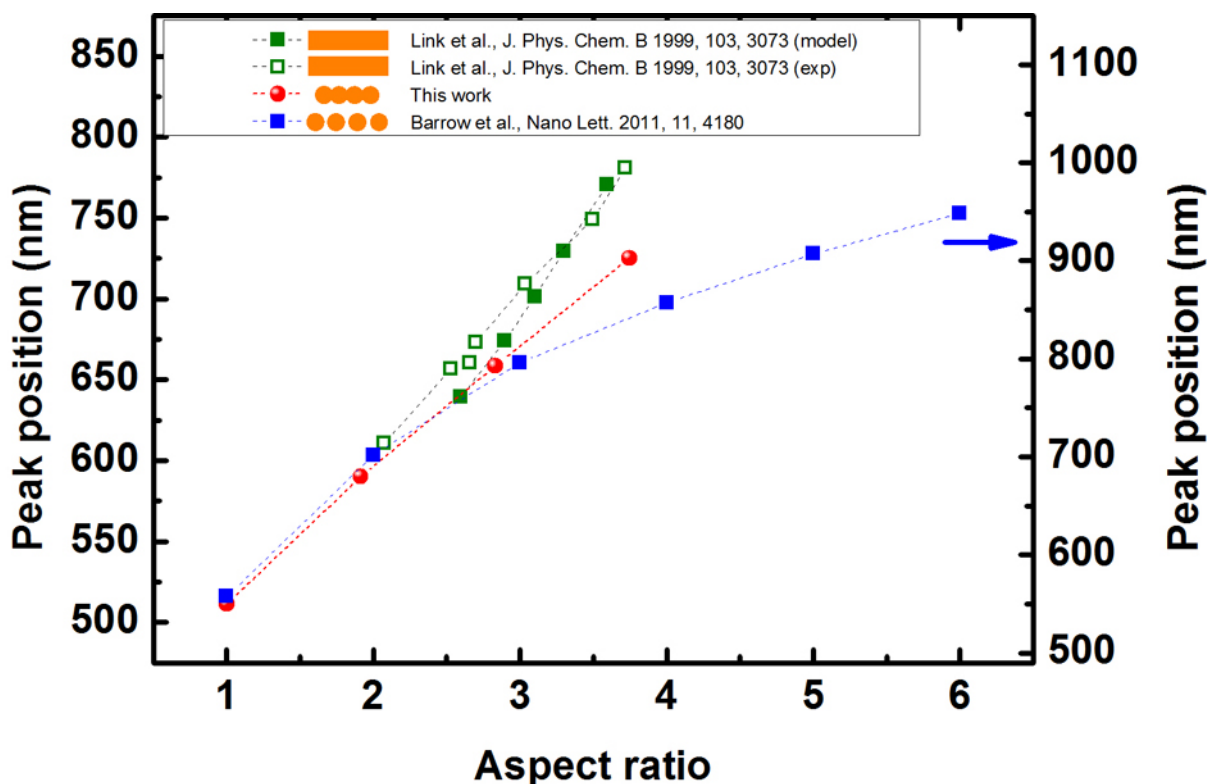


Figure S5. Comparison of the aspect ratio evolution of the longitudinal peak resonance in Au nanorods,¹⁴ short and linear nanoparticle chains¹⁵ and fused bead strings.

7. Statistical correlation between SP modes and topological features

Self-assembled, and consequently, fused PNN are complex systems, yet they are well-defined both from a synthetic viewpoint and from their optical properties viewpoint at the macroscopic level since the spectroscopic extinction signature of PNN is extremely robust.

The question of associating elementary topological configuration with specific spectroscopic features therefore naturally arises. This issue was considered in our initial work,¹ on the basis of near-field intensity.

Since EELS provides an extremely local spectroscopic probe,^{16,17} we could perform a more thorough analysis of spectra associated with basic topological patterns found in all PNN. In particular, PNN can be seen as linear chain fragments cross-linked by Y-shaped junctions and comprising a significant amount of free end chains.

Figure S6 compiles spectra associated with such topological fragments.

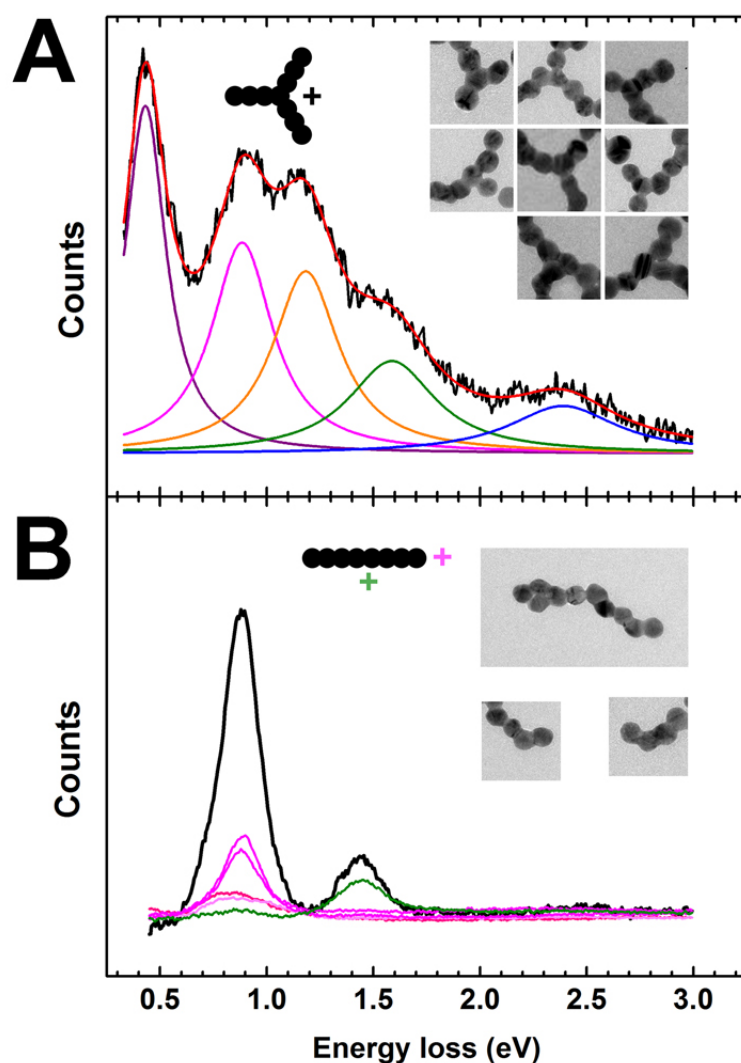


Figure S6: (A) Local EELS spectrum obtained by cumulating data specifically from Y-shaped topologies (black line). Insets: TEM images of the Y-shape fragments considered here and schematic representation of the relative position of the probe location (cross) with respect to the structures. In purple, pink, orange, green and blue lines, the five Lorentzian peaks optimized so that the sum signal (red line) fits the experimental data. (B) Global (black) and local (pink and green) EELS spectra obtained near linear chains sides (green) and ends (pink). Insets: TEM images of linear chains and free-end chains considered here and schematic representation of the relative probe position.

Spectra associated with Y-shaped junctions were systematically taken from inter-arm regions, about 10 nm from the central nanoparticle as shown by the cross in the schematic inset of Fig. S6A. These spectra exhibit multiple resonances between 2.5 and 0.5 eV, with an increasing intensity for lower energy peaks. In order to attenuate the effect of inhomogeneity in the inter-arm angles and arm lengths, spectra of Y-junctions were accumulated and are shown in Fig. S6 for a set of 8 junctions (black line). This spectrum shows five resonance features, which were associated to lorentzian peak components in agreement with previous EELS spectra analysis.¹⁸ The five lorentzian peaks that give the best fit (red line) are located at 0.43, 0.88, 1.18, 1.59 and 2.39 eV with respective quality factors of 2.10, 2.71, 3.31, 3.29 and 3.94.

The low quality factors are consistent with the residual roughness of the fused nanoparticle chain morphology. It also indicates that merging fused linear chains into a Y junction might favour the emergence of a very low resonance below 0.5 eV, which was not observed in smooth nanorods or in small dendritic nanoparticles.¹⁸

Indeed, Figure S6B shows spectra associated with linear chains. Experimental frequency-domain spectra of the whole chain exhibit three main peaks at 0.9, 1.5 and 2.5 eV, with intensity increasing rapidly towards lower energy. This is in qualitative agreement with similar spectra of Au nanorods. No peak is found below 0.5 eV. Interestingly, local spectra taken near the central edge of the chain (green cross in schematic inset and green spectra) are predominantly composed of a single peak at 1.5 eV, while local spectra taken near the chain free end (pink cross in inset and pink spectra) contribute mainly to the 0.9 eV feature. This is similar to the excitation of second- and first harmonic plasmon modes, respectively in nanorods (See Fig. 1 in reference¹⁸)

This statistical analysis suggest that the complex LDOS spectra probed by EELS do result from the contribution of specific basic topological units (Y-shaped junctions, free ends and linear fragments) that can often be associated to specific resonances (0.4 eV, 0.9 eV and 1.5 eV respectively).

However, the extreme sensitivity of the LDOS to the specific local arrangement of fused nanoparticles does not permit to build up a simple tinker toy toolbox with which a global spectral signature could be decomposed univocally into a set of elementary topological features.

In fused PNN, the entire complex object should be taken into consideration.

Therefore, we provide more maps of extra PNN that were investigated in Figure S7.

In these maps, the global fusion of the network results in the emergence of long-range delocalized modes that are responsible for the highly contrasted and spectrally tunable distribution of LDOS, which reflects not only in the EELS image but ultimately also in the transmittance of the networks as illustrated in Section 4 for a simple linear chain.

In particular, the three PNNs shown in Panels A₁-A₃ show bright and localized EELS intensity spots that are markedly displaced upon switching the excitation energy from ca. 0.6 eV (Panels B₁-B₃) to ca. 1.5 eV (Panels C₁-C₃). For the lower energies, the spatial distribution of EELS intensity is specific to each structure and varies markedly with the network topology.

Interestingly, we observe a mode convergence at higher energy. Indeed, the higher the selected energy, the more the EELS intensity distribution becomes universal and the less depend on the topology or fusion. This is well illustrated by the maps of the 2.45 eV transverse mode. While the intensity pattern follows closely the network outline, the strong confinement is uniformly distributed near the particles along the entire network for all structures (Panels D₁-D₃). Panels E₁-E₃ illustrate once more that our GDM calculations with the discrete dipole approximation

account precisely for all the details observed in the experimental maps of this higher energy mode.

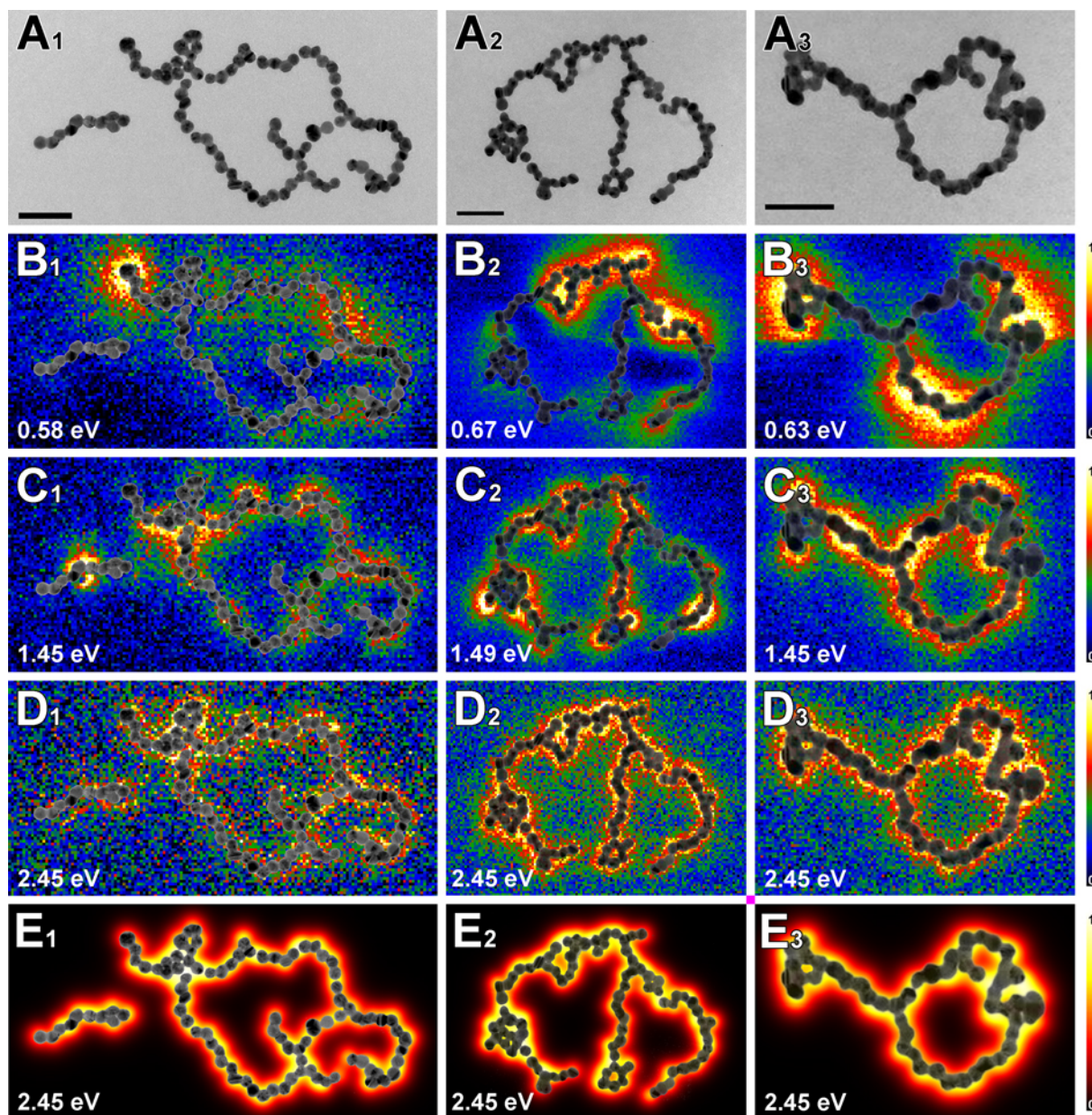


Figure S7: Mapping of plasmon modes in complex PNN. (A₁-A₃) TEM images of fused PNN with complex morphology. The small linear fragment aside in A₁ was used in the analysis of Fig. S6B. Scale bars are 50 nm. (B-D) Corresponding EELS maps recorded from the well-separated resonance features close to 0.6 eV (B₁-B₃), 1.45 eV (C₁-C₃) and at 2.45 eV (D₁-D₃), with overlaid TEM images of the fused PNN. The same color scale is used for all EELS data and shown on the right side. Data were processed as detailed in Experimental Section. (E₁-E₃) Simulated EELS map at 2.45 eV computed in the DDA approximation for each of the three structures, the TEM image of which is overlaid. The color scale is shown on the right side.

8. Principal Component Analysis

Principal component analysis is a technique to identify independent spectral features, as linearly uncorrelated "principal components" (PCs).

The first component describes the average EELS intensity in a map (a so-called Score Image), and the average of all spectra from the whole EELS spectrum image (called the first Loading spectrum). The principal components are ordered by the variance that they explain, so the subsequent second, third, etc. components (each consisting of a Score Image and a Loading Spectrum) account for decreasing amounts of spectral variance. After a certain number of extracted principal components, all significant spectral variance in the whole data set is extracted and the remaining principal components just contain random noise. More information and examples can be found in Reference ¹⁹.

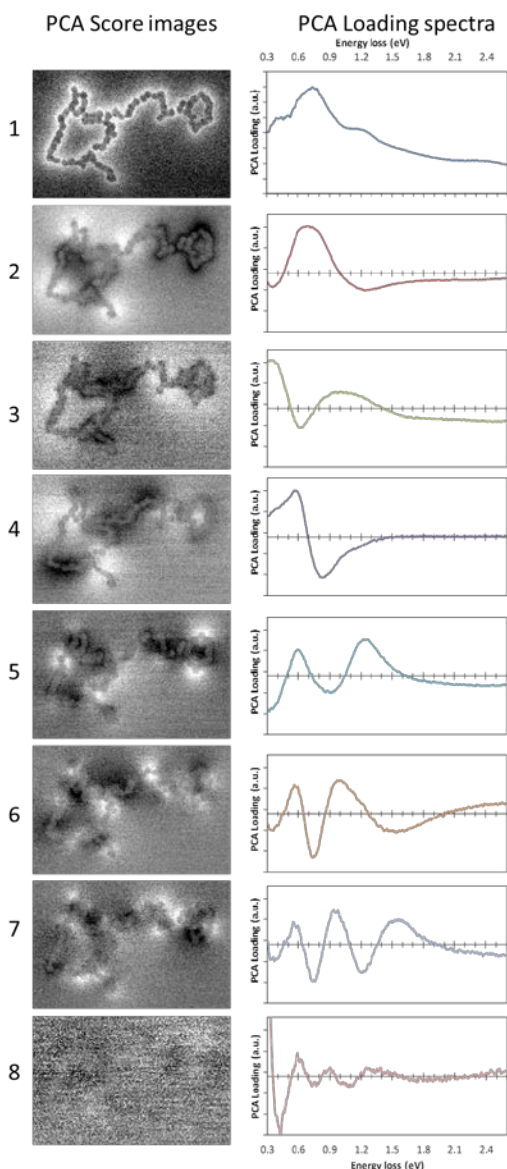


Figure S8: Principal Component Analysis of the fused PNN presented in Figure 3

In Figure S9, the PCA results are presented from the spectrum image of the fused PNN presented in Figure 3. The Score Image and Loading Spectrum of the first eight PCs are shown.

From the first PC, it can be seen that the main plasmon peaks occur at 0.4 eV, 0.6-0.8 eV, 1.1 eV and 2.4 eV but the second PC indicates that the 0.6-0.8 eV peaks are stronger but spatially anti-correlated to the other peaks. Note that the Loading Spectrum of the second PC shows which part of the energy range is higher or lower compared to the average spectrum. This confirms our interpretation of Figure S6 in which Y-shaped junctions, linear chains and chain ends contributed differently to the global spectrum, with a linear section and free-end chains indeed contributing more to this component.

The third PC extracts plasmon peaks around 0.4 eV and 1.0 eV (white in the Score Image). Thus, the third and following PCs extract a mix of several plasmon modes, the energies of which are partially overlapping. The eighth and higher PCs mainly extract the random noise in the data set.

This analysis confirms that the number of plasmon modes in our data sets is high with a distinct spatial distribution for the different groups of resonances, which are related to specific local network topologies, in full agreement with our direct analysis of the EELS maps (Figs. 1, 3, 4, S6, S7).

This wealth of both localized and delocalized modes in fused PNN offers a unique opportunity for ultimate waveguide engineering.

9. TEM and EELS map of a 0.7 μm long PNN fragment for energy loss between 0.35 and 2.45 eV

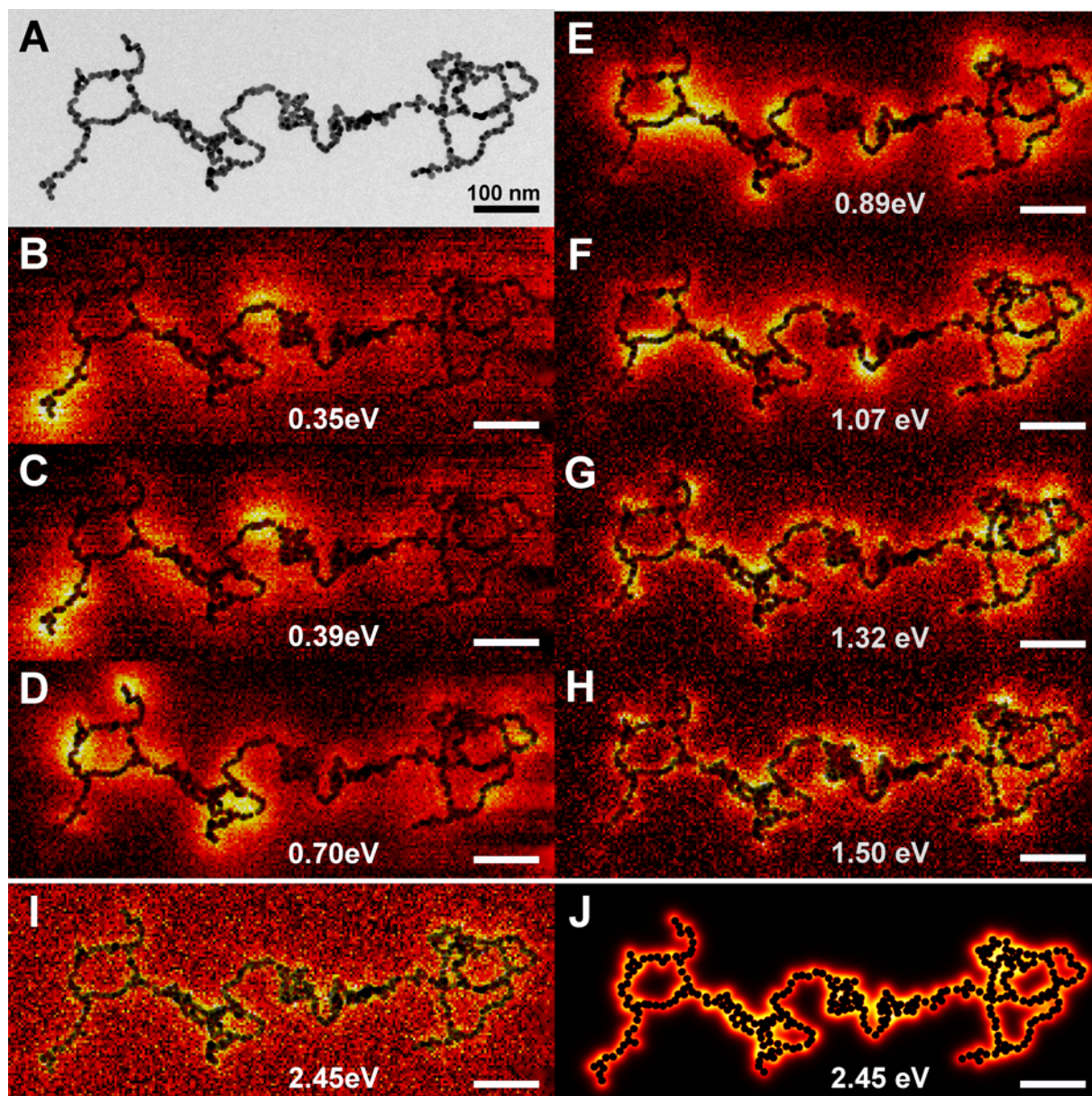


Figure S9. Plasmon delocalization in extended PNN. (A) TEM and (B-H) EELS map with TEM overlay of a large nanoparticle chain network recorded at (B) 0.35 eV (3540 nm), (C) 0.39 eV (3180 nm), (D) 0.70 eV (1770 nm), (E) 0.89 eV (1400 nm), (F) 1.07 eV (1160 nm), (G) 1.32 eV (940 nm), (H) 1.50 eV (830 nm). (I) 2.45 eV (506 nm). (J) Simulated EELS map at 2.45 eV. Scale bars: 100 nm. Color scale is similar to Fig. 3B.

EELS mapping in extended fused PNN networks such as the one shown in Fig. S9 shows that low energy modes are characterized by a contrasted series of intense spots located across the entire network. The spatial distribution is significantly modulated as the loss energy is tuned

(Panels A-H) with a tendency to be more tightly confined along the particles and more evenly distributed along the chains as the energy reaches the transverse mode at 2.45 eV (Panel I).

The transverse movement of the electrons in this mode is, to a large extent, impervious to the fusion of the particles. This case is thus faithfully accounted for by DDA-type calculations in which the individual nanoparticles are assimilated to point-like dipoles coupled to each other as shown in panel J. The match between experimental (Panel I) and simulated (Panel J) data is excellent. Although, our GDM-based simulation tool is, in principle, able to yield images corresponding to Panels A-H, the required discretization level for these extremely narrow chains combined with the large network size prevents this calculation, due to extremely long computation time.

References

1. Lin, S., Li, M., Dujardin, E., Girard, C. & Mann, S. One-dimensional plasmon coupling by facile self-assembly of gold nanoparticles into branched chain networks. *Advanced Materials* **17**, 2553-2559 (2005).
2. Li, M., Johnson, S., Guo, H. T., Dujardin, E. & Mann, S. A Generalized Mechanism for Ligand-Induced Dipolar Assembly of Plasmonic Gold Nanoparticle Chain Networks. *Advanced Functional Materials* **21**, 851-859 (2011).
3. Bosman, M. & Keast, V. J. Optimizing EELS acquisition. *Ultramicroscopy* **108**, 837-846 (2008).
4. Martin, O. J. F., Girard, C. & Dereux, A. Generalized Field Propagator for Electromagnetic Scattering and Light Confinement. *Physical Review Letters* **74**, 526-529 (1995).
5. Girard, C., Dujardin, E., Li, M. & Mann, S. Theoretical near-field optical properties of branched plasmonic nanoparticle networks. *Physical Review Letters* **97**, 100801 (2006).
6. Bonell, F. et al. Processing and near-field optical properties of self-assembled plasmonic nanoparticle networks. *Journal of Chemical Physics* **130**, 034702 (2009).
7. Girard, C. & Quidant, R. Near-field optical transmittance of metal particle chain waveguides. *Optics Express* **12**, 6141-6146 (2004).
8. de Abajo, F. J. G. & Kociak, M. Probing the photonic local density of states with electron energy loss spectroscopy. *Physical Review Letters* **100**, 106804 (2008).
9. Cohen-Tannoudji, C., Diu, B. & Laloë, F. *Quantum Mechanics* (Wiley, New York, 1977).
10. Girard, C. Near fields in nanostructures. *Reports on Progress in Physics* **68**, 1883-1933 (2005).
11. Girard, C., Dujardin, E., Marty, R., Arbouet, A. & des Francs, G. C. Manipulating and squeezing the photon local density of states with plasmonic nanoparticle networks. *Physical Review B* **81**, 153412 (2010).
12. Girard, C., Dujardin, E., Baffou, G. & Quidant, R. Shaping and manipulation of light fields with bottom-up plasmonic structures. *New Journal of Physics* **10** (2008).
13. Johnson, P. B. & Christy, R. W. Optical Constants of Noble Metals. *Physical Review B* **6**, 4370-4379 (1972).
14. Link, S., Mohamed, M. B. & El-Sayed, M. A. Simulation of the optical absorption spectra of gold nanorods as a function of their aspect ratio and the effect of the medium dielectric constant. *Journal of Physical Chemistry B* **103**, 3073-3077 (1999).
15. Barrow, S. J., Funston, A. M., Gomez, D. E., Davis, T. J. & Mulvaney, P. Surface Plasmon Resonances in Strongly Coupled Gold Nanosphere Chains from Monomer to Hexamer. *Nano Letters* **11**, 4180-4187 (2011).
16. Batson, P. E. Inelastic-scattering of fast electrons in clusters of small spheres. *Surface Science* **156**, 720-734 (1985).
17. Batson, P. E. Parallel detection for high-resolution electron-energy loss studies in the scanning-transmission electron-microscope. *Review of Scientific Instruments* **59**, 1132-1138 (1988).
18. Bosman, M. et al. Surface Plasmon Damping Quantified with an Electron Nanoprobe. *Scientific Reports* **3** (2013).
19. Bosman, M., Watanabe, M., Alexander, D. T. L. & Keast, V. J. Mapping chemical and bonding information using multivariate analysis of electron energy-loss spectrum images. *Ultramicroscopy* **106**, 1024-1032 (2006).